Article

Radiomic and Artificial Intelligence Analysis with Textural Metrics Extracted by Contrast-Enhanced Mammography and Dynamic Contrast Magnetic Resonance Imaging to Detect Breast Malignant Lesions

Roberta Fusco [1], Elio Di Bernardo [1], Adele Piccirillo [2], Maria Rosaria Rubulotta [3], Teresa Petrosino [3], Maria Luisa Barretta [3], Mauro Mattace Raso [3], Paolo Vallone [3], Concetta Raiano [3], Raimondo Di Giacomo [4], Claudio Siani [4], Franca Avino [4], Giosuè Scognamiglio [5], Maurizio Di Bonito [5], Vincenza Granata [3,*,†] and Antonella Petrillo [3,†]

[1] Medical Oncolody Division, Igea SpA, 80013 Naples, Italy; r.fusco@igeamedical.com (R.F.); e.dibernardo@igeamedical.com (E.D.B.)
[2] Department of Electrical Engineering and Information Technologies, Università degli Studi di Napoli Federico II, 80125 Naples, Italy; adelepiccirillo@gmail.com
[3] Radiology Division, Istituto Nazionale Tumori-IRCCS-Fondazione G. Pascale, 80131 Naples, Italy; m.rubulotta@istitutotumori.na.it (M.R.R.); t.petrosino@istitutotumori.na.it (T.P.); m.barretta@istitutotumori.na.it (M.L.B.); m.mattaceraso@istitutotumori.na.it (M.M.R.); p.vallone@istitutotumori.na.it (P.V.); c.raiano@istitutotumori.na.it (C.R.); a.petrillo@istitutotumori.na.it (A.P.)
[4] Senology Surgical Division, Istituto Nazionale Tumori-IRCCS-Fondazione G. Pascale, 80131 Naples, Italy; r.digiacomo@istitutotumori.na.it (R.D.G.); c.siani@istitutotumori.na.it (C.S.); f.avino@istitutotumori.na.it (F.A.)
[5] Pathology Division, Istituto Nazionale Tumori-IRCCS-Fondazione G. Pascale, 80131 Naples, Italy; g.scognamiglio@istitutotumori.na.it (G.S.); m.dibonito@istitutotumori.na.it (M.D.B.)
* Correspondence: v.granata@istitutotumori.na.it; Tel.: +39-081-590-714; Fax: +39-081-590-3825
† These authors contributed equally to this work.

Abstract: Purpose: The purpose of this study was to discriminate between benign and malignant breast lesions through several classifiers using, as predictors, radiomic metrics extracted from CEM and DCE-MRI images. In order to optimize the analysis, balancing and feature selection procedures were performed. **Methods**: Fifty-four patients with 79 histo-pathologically proven breast lesions (48 malignant lesions and 31 benign lesions) underwent both CEM and DCE-MRI. The lesions were retrospectively analyzed with radiomic and artificial intelligence approaches. Forty-eight textural metrics were extracted, and univariate and multivariate analyses were performed: non-parametric statistical test, receiver operating characteristic (ROC) and machine learning classifiers. **Results**: Considering the single metrics extracted from CEM, the best predictors were KURTOSIS (area under ROC curve (AUC) = 0.71) and SKEWNESS (AUC = 0.71) calculated on late MLO view. Considering the features calculated from DCE-MRI, the best predictors were RANGE (AUC = 0.72), ENERGY (AUC = 0.72), ENTROPY (AUC = 0.70) and GLN (gray-level nonuniformity) of the gray-level run-length matrix (AUC = 0.72). Considering the analysis with classifiers and an unbalanced dataset, no significant results were obtained. After the balancing and feature selection procedures, higher values of accuracy, specificity and AUC were reached. The best performance was obtained considering 18 robust features among all metrics derived from CEM and DCE-MRI, using a linear discriminant analysis (accuracy of 0.84 and AUC = 0.88). **Conclusions:** Classifiers, adjusted with adaptive synthetic sampling and feature selection, allowed for increased diagnostic performance of CEM and DCE-MRI in the differentiation between benign and malignant lesions.

Keywords: contrast-enhanced mammography; magnetic resonance imaging; image enhancement; contrast media; radiomics; artificial intelligence

1. Introduction

In the screening, detection and follow-up of breast cancer, the mammography (MX) was considered the first imaging examination [1,2]. In particular, thanks to the technological improvements achieved by combining digital mammography with techniques that allow low and high energy images to be obtained, and with the administration of iodate contrast agent, it is possible to acquire images that emphasize the vascularity linked to malignant lesions by the contrast agent enhancement. This imaging technique is recognized as contrast-enhanced mammography and exploits the same physiological mechanisms as dynamic contrast-enhanced magnetic resonance imaging (DCE-MRI).

DCE-MRI is an important complementary diagnostic imaging technique that was validated in the screening of high-risk women and dense breasts and in the monitoring of oncological therapies, thanks to its capability of combining morphological and functional information [2,3].

Previous studies have evaluated the sensitivity of CEM compared to conventional digital MX, ultrasound (US) and MRI [4–8]. CEM sensitivity has been reported in the range of 90–100% [5–7], which is significantly higher than the sensitivity of MX or US alone [4–7]. Moreover, CEM allows for the identification of additional occult cancers via mammography to more accurately assess the disease extent, and to guide surgical and treatment planning [8–12].

Radiomics and artificial intelligence approaches have been extensively applied to process both CEM and DCE-MRI in order to increase diagnostic performance in the detection of malignant breast lesions [13,14]. By means of the radiomics approach, it is possible to obtain, from medical images, a large amount of quantitative data that, combined with pattern recognition procedures, allow for the resolution of many clinical issues with high accuracy. Examples of features used in the oncology field are tumor size and shape, as well as intensity, statistical and textural metrics [15–42].

In this study, we designed several classifiers with the aim of discriminating between benign and malignant breast lesions using, as predictors, radiomic metrics extracted from CEM and DCE-MRI images. In order to optimize the analysis, balancing and feature selection procedures were performed.

2. Methods

2.1. Patient Selection

Patients were enrolled in this study, which was approved by the local ethical committee of National Cancer Institute of Naples Pascale Foundation. Fifty-four patients (mean age 54.3, range 31–78 years) with 79 histo-pathologically proven breast lesions (48 malignant lesions and 31 benign lesions) (Table 1) underwent both CEM and DCE-MRI. The lesions were retrospectively analyzed with radiomic and artificial intelligence approaches. Breast lesions were categorized based on the American Joint Committee on Cancer staging.

Table 1. Number and corresponding percentage of the total benign or malignant breast lesions.

Benign (31 Lesions)	Number	Percentage Value (%)
Fibrosis	6	19.35
Ductal hyperplasia	8	25.81
Fibroadenoma	9	29.03
Dysplasia	4	12.90
Adenosis	4	12.90
Malignant (48 Lesions)	**Number**	**Percentage Value (%)**
Infiltrating lobular carcinoma	7	14.58
Infiltrating ductal carcinoma	30	62.50
Ductal carcinoma in situ	9	18.75
Tubular Carcinoma	2	4.17

All women gave their written informed consent according to local ethical committee regulations.

Inclusion criteria: patient with known, histologically proven breast lesions who underwent both dual-energy CEM in craniocaudal (CC) and mediolateral oblique (MLO) views and DCE-MRI.

Exclusion criteria were previously reported in [43,44].

2.2. Imaging Protocol

CEM was acquired with the dual-energy mammography system (Hologic's Selenia® Dimensions® Unit, Bedford, MA, USA) as reported in our previous studies [43]. Two minutes after the administration of 1.5 mL/kg body weight of iodinated contrast medium (Visipaque 320; GE Healthcare, Inc., Princeton, NJ, USA) at a rate of 2–3 mL/s, each woman was placed in a CC view. Four and eight minutes after administration of the contrast agent, each breast was compressed in the MLO view: early MLO and late MLO views, respectively.

DCE-MRI was acquired with a 1.5T MR scanner (Magnetom Symphony; Siemens Medical System, Erlangen, Germany) equipped with a dedicated breast coil with 16 channels. Scan settings are reported in our previous study [44]: one series before and nine series after the automatic intravenous injection of 0.1 mmol/kg body weight of a positive paramagnetic contrast material (Gd-DOTA; Dotarem, Guerbet, Roissy CdG CEDEX, France) were acquired.

2.3. Image Processing

Regions of interest were manually segmented, slice by slice, by two expert radiologists, with 25 and 20 years of experience in breast imaging, respectively.

Breast lesions were segmented on dual-energy subtracted images, where contrast uptake was emphasized, both in CC and in MLO, and on the third T1-weighted subtracted series where contrast uptake was emphasized.

Radiomics features were extracted using the Texture Toolbox of MATLAB®, realized by Vallières et al. [45], which includes 48 parameters calculated according to the Image Biomarker Standardization Initiative [46], as previously described in [43,44]. The textural features include both first-order and second-order features; an extra detailed description of each feature has been provided in Appendix A.

2.4. Statistical Analysis

The statistical analysis was performed with RStudio software [47].

To assess variability among radiomic feature values, the intra-class correlation coefficient (ICC) was calculated. A non-parametric Wilcoxon–Mann–Whitney test and receiver operating characteristic (ROC) analysis were performed and the Youden index was calculated to obtain the optimal cut off value for each feature; then, in order to assess analysis results, the area under the ROC curve (AUC), sensitivity (SENS), specificity (SPEC), positive predictive value (PPV), negative predictive value (NPV) and accuracy (ACC) were computed.

Linear classifier (linear discriminant analysis—LDA), decision tree (TREE), k-nearest neighbors (KNN), artificial neural network (NNET) and support vector machine (SVM) using all extracted metrics of textural parameters were used [14]. Configuration settings for each classifier are provided in our previous study [41,43]. The 10-fold cross validation (10-fold CV) and the leave-one-out cross validation (LOOCV) approaches and median values of AUC, accuracy, sensitivity, specificity, PPV and NPV were obtained.

Feature selection with the least absolute shrinkage and selection operator (LASSO) method [48] was performed considering both the λ value with the minimum mean squared error (minMSE) and the largest λ value within one standard error of it (1SE) [49].

In addition, the self-adaptive synthetic over-sampling (SASYNO) approach and the adaptive synthetic sampling (ADASYN) approach, to help balance the classes (malignant and benign), were used [50–55].

The best model was chosen considering the highest area under the ROC curve and highest accuracy.

A *p*-value < 0.05 was considered as significant.

3. Results

The time interval between CEM and DCE-MRI was 2.5 days as a median value (range 1–16 days).

Table 2 reports the diagnostic performance of significant textural parameters for DCE-MRI and for dual-energy CEM in all views (i.e., CC, early and late MLO view), expressed in terms of AUC and *p*-value. The best result, considering the single feature in a univariate approach, was reached by the energy, range and GLN_GLRLM extracted on DCE-MRI volume with an AUC of 0.72.

Table 2. Accuracy of significant textural parameters for DCE-MRI and for dual-energy CEM CC, early and late MLO view.

Mammography Projection	Textural Parameters	AUC Values	*p*-Value
CC-view	IQR	0.67	0.01
	Variance	0.68	0.01
	Correlation	0.69	0.000
MLO view	Kurtosis	0.71	0.000
	Skewness	0.71	0.000
Magnetic Resonance Images	Textural Parameters	AUC Values	*p*-Value
	Range	0.72	0.001
	Energy	0.72	0.001
	Entropy	0.70	0.003
	GLN_GLRLM	0.72	0.001
	GLN_GLSZM	0.70	0.002

Figure 1 shows ROC curve trends of significant textural features: variance, correlation and IQR for mammography CC projection, kurtosis and skewness for mammography early-MLO projection and range, energy, entropy, GLN_GLRLM and GLN_GLSZM for DCE-MRI images.

Figure 2 shows the boxplots related to the above-mentioned parameters, to separate benign from malignant lesions.

Table 3 reports the performance achieved by the best classifiers designed to discriminate between benign and malignant lesions using CEM and DCE-MRI images.

The best performance, considering the CC view (ACC = 0.71; SENS = 0.71; SPEC = 0.71; PPV = 0.71; NPV = 0.71; AUC = 0.77), was reached with an SVM trained with 10-fold CV and balanced data (with SASYNO function) and a subset of four features (by LASSO and λminMSE). The subset of four robust textural features includes IQR, VARIANCE, CORRELATION and RLV.

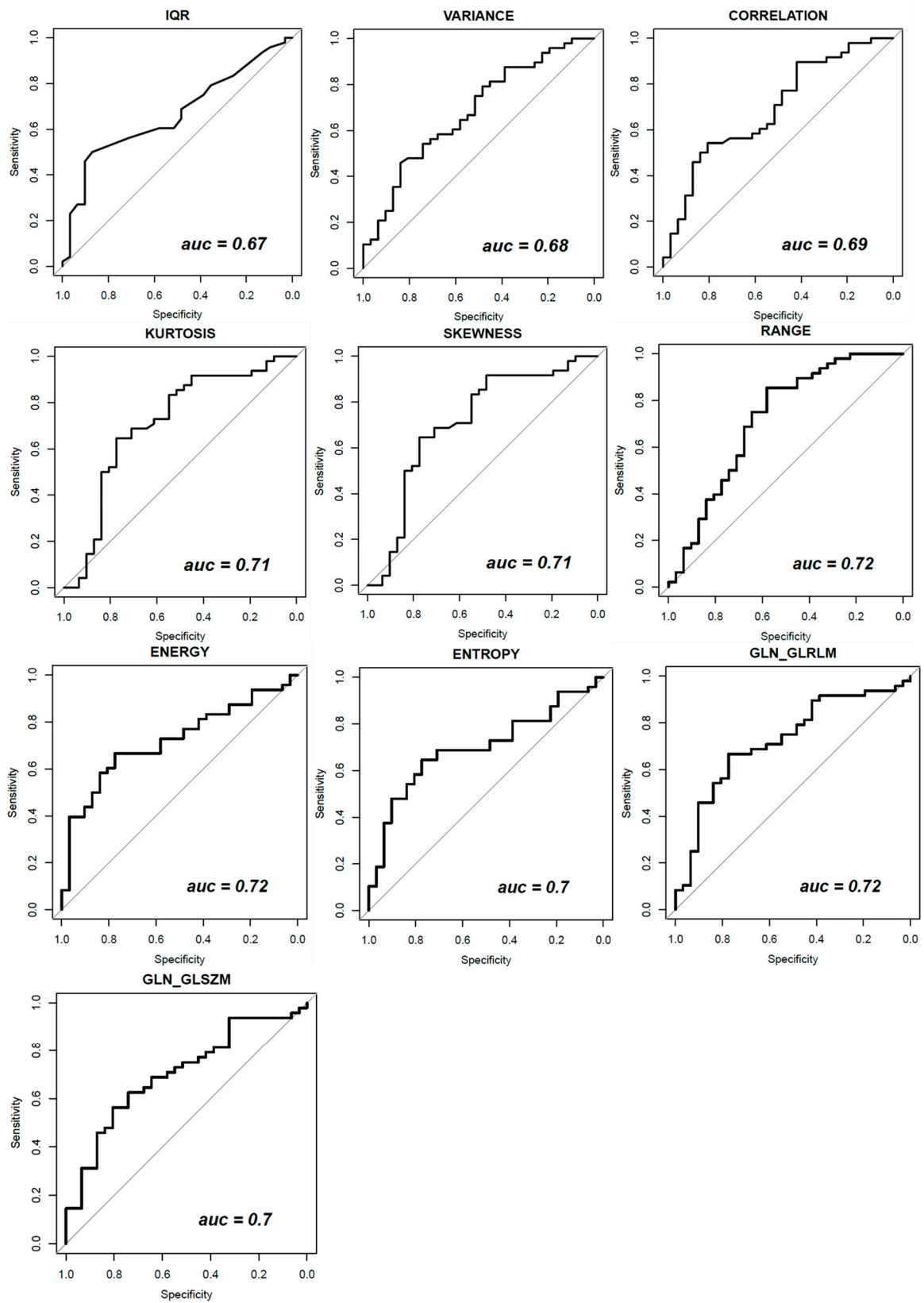**Figure 1.** ROC curve trends of significant textural features for DCE-MRI and for dual-energy CEM CC, early and late MLO view.
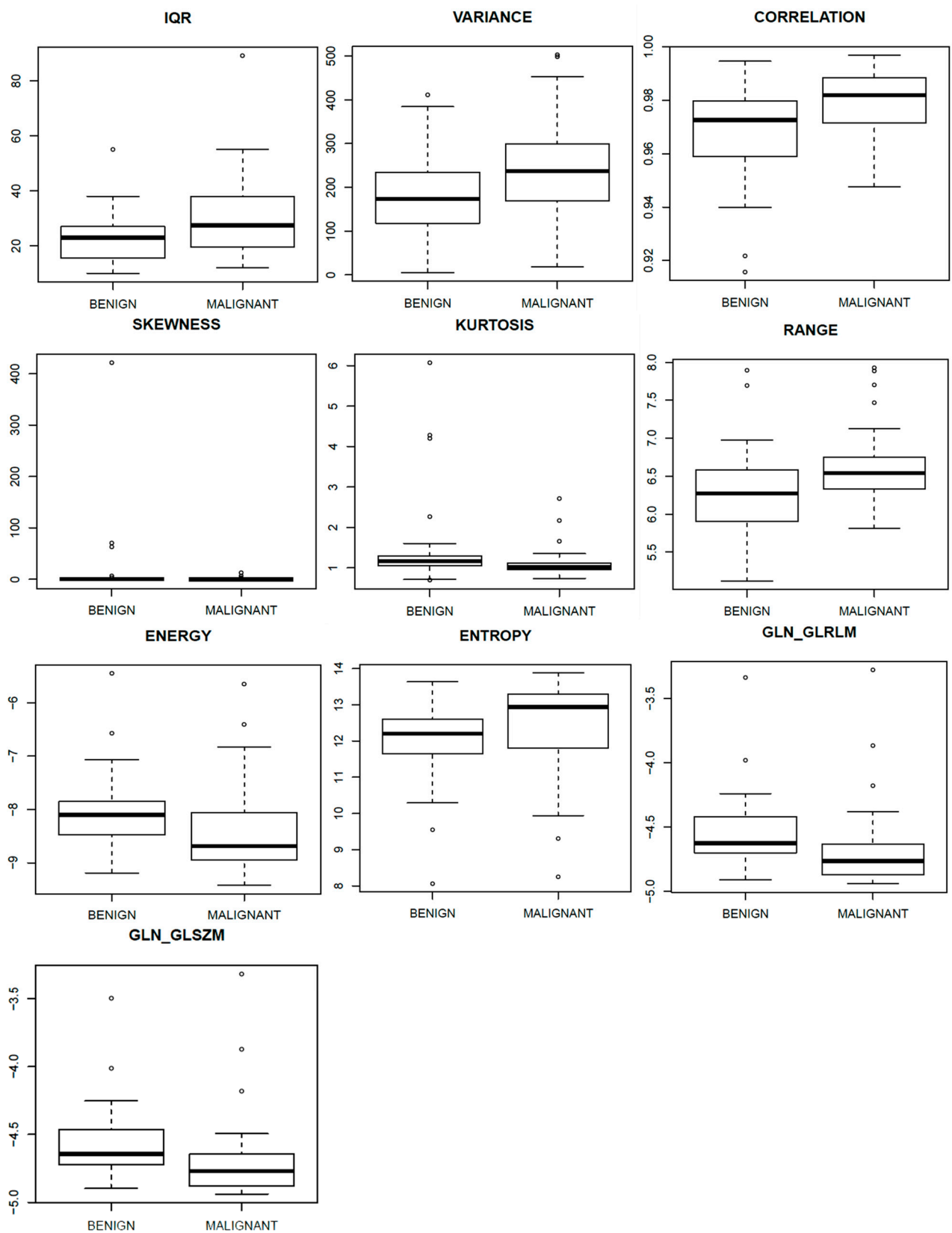
Figure 2. Boxplots of significant textural features for DCE-MRI and for dual-energy CEM CC, early and late MLO view.

Table 3. Performance of the best classifiers designed to discriminate between benign and malignant lesions.

Classifier	Cross-Validation	ACC	SENS	SPEC	PPV	NPV	AUC
CEM–CC view							
Performance of classifiers trained with balanced data (with ADASYN function) and a subset of 34 textural features (AUC ≥ 0.60).							
TREE	10-fold CV	0.74	0.74	0.78	0.76	0.74	0.73
Performance of classifiers trained with balanced data (with SASYNO function) and a subset of 4 robust textural features (by LASSO and λ_{minMSE}).							
LDA	10-fold CV	0.71	0.71	0.71	0.71	0.71	0.76
	LOOCV	0.71	0.71	0.71	0.71	0.71	0.75
SVM	10-fold CV	0.71	0.71	0.71	0.71	0.71	0.77
Performance of classifiers trained with balanced data (with SASYNO function) and a subset of 3 robust textural features (by LASSO and λ_{1SE}).							
LDA	10-fold CV	0.71	0.71	0.71	0.71	0.71	0.76
	LOOCV	0.71	0.71	0.71	0.71	0.71	0.75
NNET	10-fold CV	0.70	0.71	0.69	0.69	0.70	0.74
	LOOCV	0.70	0.73	0.67	0.69	0.71	0.74
SVM	10-fold CV	0.71	0.71	0.71	0.71	0.71	0.75
	LOOCV	0.72	0.73	0.71	0.71	0.72	0.76
CEM–early MLO view							
Performance of classifiers trained with balanced data (with ADASYN function) and all 48 textural features							
LDA	10-fold CV	0.76	0.65	0.87	0.82	0.74	0.73
	LOOCV	0.75	0.60	0.87	0.81	0.72	0.71
Performance of classifiers trained with balanced data (with ADASYN function) and a subset of 7 robust textural features (by LASSO and λ_{minMSE}).							
LDA	10-fold CV	0.66	0.54	0.75	0.65	0.65	0.72
	LOOCV	0.66	0.56	0.75	0.66	0.66	0.7
Performance of classifiers trained with balanced data (with ADASYN function) and a subset of 14 robust textural features (by LASSO and λ_{1SE}).							
LDA	10-fold CV	0.62	0.52	0.69	0.60	0.62	0.71
	LOOCV	0.66	0.56	0.75	0.66	0.66	0.7
CEM–late MLO view							
Performance of classifiers trained with balanced data (with ADASYN function) and all 48 textural features							
LDA	10-fold CV	0.78	0.71	0.84	0.79	0.77	0.78
	LOOCV	0.78	0.69	0.86	0.80	0.76	0.77

Table 3. *Cont.*

Classifier	Cross-Validation	ACC	SENS	SPEC	PPV	NPV	AUC
		CEM–late MLO view					
Performance of classifiers trained with balanced data (with ADASYN function) and a subset of 17 robust textural features (by LASSO and λ_{minMSE}).							
LDA	10-fold CV	0.75	0.71	0.77	0.72	0.75	0.8
	LOOCV	0.73	0.71	0.75	0.71	0.75	0.8
NNET	10-fold CV	0.72	0.65	0.77	0.70	0.72	0.78
	LOOCV	0.72	0.69	0.75	0.70	0.74	0.72
Performance of classifiers trained with balanced data (with ADASYN function) and a subset of 14 robust textural features (by LASSO and λ_{1SE}).							
LDA	10-fold CV	0.71	0.69	0.71	0.67	0.73	0.78
	LOOCV	0.70	0.69	0.71	0.67	0.73	0.78
NNET	10-fold CV	0.71	0.67	0.75	0.70	0.72	0.74
	LOOCV	0.74	0.69	0.79	0.73	0.75	0.74
		CEM–CC + early MLO + late view					
Performance of classifiers trained with balanced data (with ADASYN function) and a subset of 15 robust textural features (by LASSO and λ_{minMSE}).							
LDA	10-fold CV	0.75	0.69	0.81	0.77	0.75	0.82
	LOOCV	0.76	0.71	0.81	0.77	0.76	0.81
NNET	10-fold CV	0.77	0.75	0.80	0.77	0.78	0.79
	LOOCV	0.79	0.75	0.81	0.78	0.79	0.81
SVM	10-fold CV	0.72	0.73	0.70	0.69	0.75	0.79
	LOOCV	0.76	0.73	0.80	0.76	0.77	0.81
Performance of classifiers trained with balanced data (with ADASYN function) and a subset of 8 robust textural features (by LASSO and λ_{1SE}).							
NNET	10-fold CV	0.72	0.73	0.72	0.70	0.75	0.78
		DCE-MRI					
Performance of classifiers trained with balanced data (with ADASYN function) and all 48 textural features							
LDA	10-fold CV	0.73	0.69	0.77	0.73	0.73	0.71
	LOOCV	0.70	0.65	0.75	0.70	0.70	0.7
Performance of classifiers trained with balanced data (with SASYNO function) and a subset of 15 robust textural features (by LASSO and λ_{minMSE}).							
SVM	10-fold CV	0.74	0.73	0.75	0.74	0.73	0.72
	LOOCV	0.70	0.69	0.71	0.70	0.69	0.71

The best performance, considering the early-MLO view (ACC = 0.76; SENS = 0.65; SPEC = 0.87; PPV = 0.82; NPV = 0.74; AUC = 0.73), was reached with an LDA trained with 10-fold CV and trained with balanced data (with ADASYN function) and all 48 textural features.

The best performance, considering the late-MLO view (ACC = 0.75; SENS = 0.71; SPEC = 0.77; PPV = 0.72; NPV = 0.75; AUC = 0.80), was reached with an LDA trained with 10-fold CV and balanced data (with ADASYN function) and a subset of 17 features (by LASSO). The subset of 17 robust textural features includes MEAN, MODE, MAD, RANGE,

VARIANCE, CONTRAST, CORRELATION, SRLGE, LRLGE, RLV, SZE, SZLGE, SZHGE, GLV_GLSZM, BUSYNESS, COMPLEXITY and STRENGTH.

The best performance, considering all three mammographic projections (ACC = 0.79; SENS = 0.75; SPEC = 0.81; PPV = 0.78; NPV = 0.79; AUC = 0.81), was reached with an NNET trained with LOOCV and balanced data (with ADASYN function) and a subset of 15 features (by LASSO). The subset of 15 robust textural features includes IQR, VARIANCE, CORRELATION, LRHGE, GLV_GLRLM and SZLGE among textural features extracted from CC view; MODE, CONTRAST and GLV_GLRLM among textural features extracted from early-MLO view; MODE, STD, RANGE, IQR, CORRELATIOND and COMPLEXITY among textural features extracted from late-MLO view.

With regard to DCE-MRI images, the best performance (ACC = 0.74; SENS = 0.73; SPEC = 0.75; PPV = 0.74; NPV = 0.73; AUC = 0.72) was reached with an SVM trained with 10-fold CV and balanced data (with SASYNO function) and a subset of 15 features (by LASSO and λminMSE). The subset of 15 robust textural features includes MODE, MEDIAN, STD, MAD, ENTROPY, SUM AVERAGE, SRE, GLN_GLRLM, SRHGE, LZE, ZSN, ZP, LZHGE, GLV_GLSZM and ZSV.

Table 4 reports the performance achieved by the best classifiers to discriminate benign from malignant lesions when features extracted from CEM and DCE-MRI were combined. The best results overall (ACC = 0.84; SENS = 0.73; SPEC = 0.92; PPV = 0.90; NPV = 0.79; AUC = 0.88) were obtained considering a subset of 18 textural features extracted from all three mammographic views (CC, early MLO and late MLO) and DCE-MRI with an LDA trained with 10-fold CV and with balanced data (with ADASYN function). The subset of 18 robust textural features (by LASSO and λminMSE) includes IQR, VARIANCE, CORRELATION, LRHGE, GLV_GLRLM and RLV among textural features extracted from CC mammographic view; MODE and CONTRAST among textural features extracted from early-MLO mammographic view; STD, RANGE, CORRELATION and COMPLEXITY among textural features extracted from late-MLO mammographic view; RANGE, KURTOSIS, AUTOCORRELATION, LRHGE, LZE and GLV_GLSZM among textural features extracted from DCE-MRI images.

Table 4. Performance achieved by the best classifiers to discriminate between benign and malignant lesions for combined CEM and DCE-MRI.

Classifier	Cross-Validation	ACC	SENS	SPEC	PPV	NPV	AUC
Performance for classifiers trained with balanced data (with ADASYN function) and a subset of 18 robust textural features (by LASSO and λ_{minMSE}).							
LDA	10-fold CV	0.84	0.73	0.92	0.90	0.79	0.88
	LOOCV	0.80	0.71	0.88	0.85	0.77	0.87
SVM	10-fold CV	0.84	0.81	0.87	0.85	0.83	0.86
	LOOCV	0.83	0.79	0.87	0.84	0.82	0.86
Performance for classifiers trained with balanced data (with SASYNO function) and a subset of 3 robust textural features (by LASSO and λ_{minMSE}).							
LDA	10-fold CV	0.79	0.79	0.79	0.79	0.79	0.88
	LOOCV	0.79	0.79	0.79	0.79	0.79	0.89
SVM	10-fold CV	0.80	0.79	0.79	0.79	0.79	0.86
	LOOCV	0.79	0.77	0.81	0.80	0.78	0.87

Figure 3 shows the ROC curves of the best classifier obtained combining features from CEM and DCE-MRI.
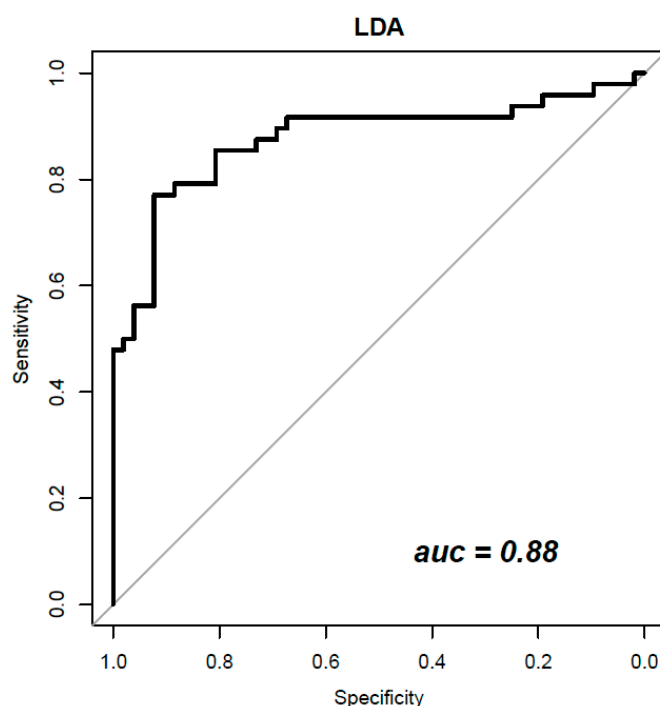
Figure 3. LDA classifier ROC curve trained with 18 robust radiomic features from CEM and DCE-MRI.

4. Discussion

Using texture features from dual-energy CEM and DCE-MRI, considered both individually and in combination, we aimed to evaluate radiomic analysis in discriminating between malignant and benign breast lesions.

In recent years, many studies have addressed the problem of breast lesion classification by using several feature categories such as textural and morphological features, in combination with different machine learning approaches, based on CEM and on DCE-MRI images analysis considered separately [30–41,56–60].

Marino et al. [61] investigated the potential of radiomic analysis of both CEM and DCE-MRI of the breast for the non-invasive assessment of tumor invasiveness, hormone receptor status and tumor grade in patients with primary breast cancer. This retrospective study included 48 female patients with 49 biopsy-proven breast cancers who underwent pretreatment breast CEM and MRI. Radiomic analysis was performed by using MaZda software. Radiomic parameters were correlated with tumor histology (invasive vs. non-invasive), hormonal status (HR+ vs. HR−) and grading (low grade G1 + G2 vs. high grade G3). CEM radiomics analysis yielded classification accuracies of up to 92% for invasive vs. non-invasive breast cancers, 95.6% for HR+ vs. HR− breast cancers and 77.8% for G1 + G2 vs. G3 invasive cancers. MRI radiomics analysis yielded classification accuracies of up to 90% for invasive vs. non-invasive breast cancers, 82.6% for HR+ vs. HR− breast cancers and 77.8% for G1 + G2 vs. G3 cancers. Their study, however, did not reported the combination of radiomic features extracted from CEM and DCE-MRI.

Jiang et al. [62] noninvasively evaluated the use of intratumoral and peritumoral regions from full-field digital mammography (DM), digital breast tomosynthesis (DBT) and dynamic contrast-enhanced and diffusion-weighted (DW) magnetic resonance imaging images separately and combined to predict the Ki-67 level based on radiomics. Their results demonstrated that the combined intra- and peritumoral radiomic signatures improved the AUC compared with the intra- or peritumoral radiomic signature in each modality. The nomogram incorporating the multi-model radiomics signature, age and lymph node metastasis status achieved the best prediction performance in the training (AUC = 0.922) and validation (AUC = 0.866) cohorts.

Zhao et al. [63] constructed radiomic models from DCE-MRI and mammography for the values in the diagnosis of breast cancer, reporting an accuracy of the individual model of 83.2% for DCE-MRI, 75.7% for mammography lesion, 64.4% for mammography margin and 77.2% for lesion + margin. When all features were combined, the accuracy increased to 89.6%.

Niu et al. [64] evaluated digital mammography, DBT, DCE- and DW-MRI, individually and combined, for the values in the diagnosis of breast cancer. They reported that the radiomic signature derived from DBT plus DM generated a lower AUC and sensitivity, but a higher specificity compared with that from DCE plus DWI. The nomogram integrating the combined radiomic signature, age and menstruation status achieved the best diagnostic performance in the training (AUC = 0.975) and validation (AUC = 0.983) cohorts.

Our results demonstrated that, considering the single metrics extracted from CEM, the best predictors were KURTOSIS (area under ROC curve (AUC) = 0.71) and SKEWNESS (AUC = 0.71) calculated on late MLO view. Considering the features calculated from DCE-MRI, the best predictors were RANGE (AUC = 0.72), ENERGY (AUC = 0.72), ENTROPY (AUC = 0.70) and GLN (Gray-Level Nonuniformity) of the gray-level run-length matrix (AUC = 0.72).

Considering the analysis with classifiers and the unbalanced dataset, no significant results were obtained. After the balancing and feature selection procedures, higher values of accuracy, specificity and AUC were reached. The best performance was obtained considering 18 robust features among all metrics derived from CEM and DCE-MRI, using a linear discriminant analysis (accuracy of 0.84 and AUC = 0.88).

This study had some limitations. The small cohort of studied patients represents a preliminary result to validate increasing the cohort of patients. Manual segmentation was time-consuming and could be operator-dependent and lose reproducibility; however, an automatic segmentation considering possible multicentric lesions or background parenchymal enhancement could be difficult to perform. In this study, the histological differences of tumors were not considered. This could improve the performance in the classification problem and allow for the classification of breast lesions according to grading and histotype.

Both DCE-MRI and CEM provide functional information on neoplastic neo-angiogenesis. CEM is an attractive alternative when MRI is not available, contraindicated or poorly tolerated. However, at our institution, a study protocol to compare DCE-MRI and CEM in staging and follow-up in breast cancer is still ongoing. Therefore, a future endpoint could be to design separate classifiers for CEM and DCE-MRI images and then merge the results in specific clinical settings, such as during patient follow-up in cases of suspicious local recurrence.

5. Conclusions

In conclusion, classifiers adjusted with adaptive synthetic sampling and feature selection allowed for increased diagnostic performance of CEM and DCE-MRI in the differentiation between benign and malignant lesions.

Institutional Review Board Statement: The study was approved by the Ethics Committee of the National Cancer Institute of Naples Pascale Foundation (Deliberation N. 617 of 9 August 2016).

Informed Consent Statement: Each patient signed the informed consent.

Appendix A. Definition of Textural Features

Appendix A.1. First-Order Gray-Level Statistics

First-order gray-level statistics describe the distribution of gray values within the volume. Let X denote the 3-D image matrix with N voxels, P the first order histogram, $P(i)$ the fraction of voxels with intensity level i and Nl the number of discrete intensity levels.

- Mean, the mean gray level of X.

$$mean = \frac{1}{N} \sum_{i=1}^{N} X(i)$$

- Mode, the most frequent element(s) of array X.
- Median, the sample median of X or the 50th percentile of X.
- Standard deviation (STD)

$$STD = \left(\frac{1}{N-1} \sum_{i=1}^{N} \left(X(i) - \overline{X} \right)^2 \right)^{1/2}$$

- Mean Absolute Deviation (MAD), the mean of the absolute deviation of all voxel intensities around the mean intensity value.

$$MAD = \frac{1}{N} \sum_{i=1}^{N} |X(i) - \overline{X}|$$

- Range, the range of intensity values of X.

$$range = \max(X) - \min(X)$$

where $\max(X)$ is the maximum intensity value of X and $\min(X)$ is the minimum intensity value of X.

- Interquartile range (IQR), the interquartile range is defined as the 75th minus the 25th percentile of X.
- Kurtosis:

$$kurtosis = \frac{\frac{1}{N} \sum_{i=1}^{N} \left(X(i) - \overline{X} \right)^4}{\left(\sqrt{\frac{1}{N} \sum_{i=1}^{N} \left(X(i) - \overline{X} \right)^2} \right)^2}$$

where $\overline{X}$ is the mean of X.

- Variance, Variance is the square of the standard deviation:

$$variance = \frac{1}{N-1} \sum_{i=1}^{N} \left(X(i) - \overline{X} \right)^2$$

where $\overline{X}$ is the mean of X.

- Skewness:

$$skewness = \frac{\frac{1}{N} \sum_{i=1}^{N} (X(i) - \overline{X})^3}{\left(\sqrt{\frac{1}{N} \sum_{i=1}^{N} (X(i) - \overline{X})^2} \right)^3}$$

where $\overline{X}$ is the mean of X.

Appendix A.2. Gray Level Co-Occurrence Matrix (GLCM)

A normalized GLCM is defined as $P(i, j; \delta, \alpha)$, a metric with size $N_g \times N_g$ describing the second-order joint probability function of an image, where the (i, j)th element represents the number of times the combination of intensity levels i and j occur in two pixels in the image, that are separated by a distance of δ pixels in direction α and N_g is the maximum discrete intensity level in the image. Let:

- $P(i, j)$ be the normalized (i.e., $\sum P(i, j) = 1$) co-occurrence matrix, generalized for any δ and α,
- $p_x(i) = \sum_{j=1}^{N_g} P(i, j)$,
- $p_y(j) = \sum_{i=1}^{N_g} P(i, j)$,
- μ_x be the mean of p_x, where $\mu_x = \sum_{i=1}^{N_g} \sum_{j=1}^{N_g} i P(i, j)$,
- μ_y be the mean of p_y, where $\mu_y = \sum_{i=1}^{N_g} \sum_{j=1}^{N_g} j P(i, j)$,
- σ_x be the standard deviation of p_x, where $\sigma_x = \sum_{i=1}^{N_g} \sum_{j=1}^{N_g} P(i, j)(i - \mu_x)^2$,
- σ_y be the standard deviation of p_y, where $\sigma_y = \sum_{i=1}^{N_g} \sum_{j=1}^{N_g} P(i, j)(j - \mu_y)^2$.

- Energy

$$energy = \sum_{i=1}^{N_g} \sum_{j=1}^{N_g} [P(i, j)]^2$$

- Contrast

$$contrast = \sum_{i=1}^{N_g} \sum_{j=1}^{N_g} |i - j|^2 P(i, j)$$

- Entropy

$$entropy = - \sum_{i=1}^{N_g} \sum_{j=1}^{N_g} P(i, j) log_2 [P(i, j)]$$

- Homogeneity

$$homogeneity = \sum_{i=1}^{N_g} \sum_{j=1}^{N_g} \frac{P(i, j)}{1 + |i - j|}$$

- Correlation

$$correlation = \frac{\sum_{i=1}^{N_g} \sum_{j=1}^{N_g} ij P(i, j) - \mu_x \mu_y}{\sigma_x \sigma_y}$$

- Sum Average

$$sum\ average = \frac{1}{N_g \times N_g} \sum_{i=1}^{N_g} \sum_{j=1}^{N_g} [i P(i, j) + j P(i, j)]$$

- Dissimilarity

$$dissimilarity = \sum_{i=1}^{N_g} \sum_{j=1}^{N_g} |i - j| P(i, j)$$

- Autocorrelation

$$autocorrelation = \sum_{i=1}^{N_g} \sum_{j=1}^{N_g} ijP(i,j)$$

Appendix A.3. Gray Level Run-Length Matrix (GLRLM)

Run-length metrics quantify gray level runs in an image. A gray level run is defined as the length in number of pixels, of consecutive pixels that have the same gray level value. In a gray level run length matrix $p(i,j|\theta)$, the (i,j)th element describes the number of times j a gray level i appears consecutively in the direction specified by θ. Let:

- $p(i,j)$ be the (i,j)th entry in the given run-length matrix p, generalized for any direction θ,
- N_g be the number of discrete intensity values in the image,
- N_r be the maximum run length,
- N_s be the total numbers of runs, where $N_s = \sum_{i=1}^{N_g} \sum_{j=1}^{N_r} p(i,j)$,
- p_r be the sum distribution of the number of runs with run length j, where $p_r(j) = \sum_{i=1}^{N_g} p(i,j)$,
- p_g be the sum distribution of the number of runs with run length i, where $p_g(i) = \sum_{j=1}^{N_r} p(i,j)$,
- N_p be the number of voxels in the image, where $N_p = \sum_{j=1}^{N_r} jp_r$,
- μ_r be the mean run length, where $\mu_r = \sum_{i=1}^{N_g} \sum_{j=1}^{N_r} jp_n(i,j)$,
- μ_g be the mean gray level, where $\mu_g = \sum_{i=1}^{N_g} \sum_{j=1}^{N_r} ip_n(i,j)$.

- Short-Run Emphasis (SRE)

$$SRE = \sum_{j=1}^{N_r} \frac{p_r}{j^2}$$

- Long-Run Emphasis (LRE)

$$LRE = \sum_{j=1}^{N_r} j^2 p_r$$

- Gray Level Nonuniformity (GLN)

$$GLN = \sum_{i=1}^{N_g} p_g{}^2$$

- Run-Length Nonuniformity (RLN)

$$RLN = \sum_{j=1}^{N_r} p_r{}^2$$

- Run Percentage (RP)

$$RP = \frac{N_s}{N_p}$$

- Low Gray Level Run Emphasis (LGRE)

$$LGRE = \sum_{i=1}^{N_g} \frac{p_g}{i^2}$$

- High Gray Level Run Emphasis (HGRE)

$$HGRE = \sum_{i=1}^{N_g} i^2 p_g$$

- Short-Run Low Gray Level Emphasis (SRLGE)

$$SRLGE = \sum_{i=1}^{N_g} \sum_{j=1}^{N_r} \frac{p(i,j)}{i^2 j^2}$$

- Short-Run High Gray Level Emphasis (SRHGE)

$$SRHGE = \sum_{i=1}^{N_g} \sum_{j=1}^{N_r} \frac{p(i,j)i^2}{j^2}$$

- Long-Run Low Gray Level Emphasis (LRLGE)

$$LRLGE = \sum_{i=1}^{N_g} \sum_{j=1}^{N_r} \frac{p(i,j)j^2}{i^2}$$

- Long-Run High Gray Level Emphasis (LRHGE)

$$LRHGE = \sum_{i=1}^{N_g} \sum_{j=1}^{N_r} p(i,j)i^2 j^2$$

- Gray Level Variance (GLV)

$$GLV = \frac{1}{N_g \times N_r} \sum_{i=1}^{N_g} \sum_{j=1}^{N_r} \left(ip(i,j) - \mu_g\right)^2$$

- Run-Length Variance (RLV)

$$RLV = \frac{1}{N_g \times N_r} \sum_{i=1}^{N_g} \sum_{j=1}^{N_r} (jp(i,j) - \mu_r)^2$$

Appendix A.4. Gray Level Size Zone Matrix (GLSZM)

A gray level size-zone matrix describes the amount of homogeneous connected areas within the volume, of a certain size and intensity. The (i, j) entry of the GLSZM $p(i, j)$ is the number of connected areas of gray level (i.e., intensity value) i and size j. GLSZM features therefore describe homogeneous areas within the tumor volume, describing tumor heterogeneity at a regional scale [5]. Let:

- $p(i, j)$ be the (i, j)th entry in the given GLSZM p,
- N_g be the number of discrete intensity values in the image,
- N_z be the size of the largest, homogeneous region in the volume of interest,
- N_s be the total number of homogeneous regions (zones), where $N_s = \sum_{i=1}^{N_g} \sum_{j=1}^{N_z} p(i,j)$,
- p_z be the sum distribution of the number of zones with size j, where $p_z(j) = \sum_{i=1}^{N_g} p(i,j)$,
- p_g be the sum distribution of the number of zones with gray level i, where $p_g(i) = \sum_{j=1}^{N_z} p(i,j)$,
- N_p be the number of voxels in the image, where $N_p = \sum_{j=1}^{N_z} jp_r$,

- μ_r be the mean zone size, where $\mu_r = \sum_{i=1}^{N_g} \sum_{j=1}^{N_z} j\,p(i,j|\theta)$,

- μ_g be the mean gray level, where $\mu_g = \sum_{i=1}^{N_g} \sum_{j=1}^{N_z} i\,p(i,j|\theta)$.

- Small Zone Emphasis (SZE)

$$SZE = \sum_{j=1}^{N_z} \frac{p_z}{j^2}$$

- Large Zone Emphasis (LZE)

$$LZE = \sum_{j=1}^{N_z} j^2 p_z$$

- Gray Level Nonuniformity (GLN)

$$GLN = \sum_{i=1}^{N_g} p_g{}^2$$

- Zone Size Nonuniformity (ZSN)

$$ZSN = \sum_{i=1}^{N_g} p_z{}^2$$

- Zone Percentage (ZP)

$$ZP = \frac{N_s}{N_p}$$

- Low Gray Level Zone Emphasis (LGZE)

$$LGZE = \sum_{i=1}^{N_g} \frac{p_g}{i^2}$$

- High Gray Level Zone Emphasis (HGZE)

$$HGZE = \sum_{i=1}^{N_g} i^2 p_g$$

- Small Zone Low Gray Level Emphasis (SZLGE)

$$SZLGE = \sum_{i=1}^{N_g} \sum_{j=1}^{N_z} \frac{p(i,j)}{i^2 j^2}$$

- Small Zone High Gray Level Emphasis (SZHGE)

$$SZHGE = \sum_{i=1}^{N_g} \sum_{j=1}^{N_z} \frac{p(i,j)i^2}{j^2}$$

- Large Zone Low Gray Level Emphasis (LZLGE)

$$LZLGE = \sum_{i=1}^{N_g} \sum_{j=1}^{N_z} \frac{p(i,j)j^2}{i^2}$$

- Large Zone High Gray Level Emphasis (LZHGE)

$$LZHGE = \sum_{i=1}^{N_g} \sum_{j=1}^{N_z} p(i,j)j^2 i^2$$

- Gray Level Variance (GLV)

$$GLV = \frac{1}{N_g \times N_z} \sum_{i=1}^{N_g} \sum_{j=1}^{N_z} \left(ip(i,j) - \mu_g\right)^2$$

- Zone Size Variance (ZSV)

$$ZSV = \frac{1}{N_g \times N_z} \sum_{i=1}^{N_g} \sum_{j=1}^{N_z} \left(jp(i,j) - \mu_z\right)^2$$

Appendix A.5. Neighborhood Gray Tone Difference Matrix (NGTDM)

The ith entry of the NGTDM $s(i|d)$ is the sum of gray level differences of voxels with intensity i and the average intensity A_i of their neighboring voxels within a distance d. Let:

- n_i be the number of voxels with gray level i,
- $N = \sum n_i$ be the total number of voxels,
- $s(i) = \begin{cases} \sum_{n_i} |i - A_i| \ for \ n_i > 0 \\ 0 \ otherwise \end{cases}$ be generalized for any distance d,
- N_g be the maximum discrete intensity level in the image,
- $p(i) = \frac{n_i}{N}$ be the probability of gray level i,
- N_p be the total number of gray levels present in the image.

- Coarseness:

$$coarseness = \left[\varepsilon + \sum_{n=1}^{N_g} p(i)s(i)\right]^{-1}$$

where ε is a small number to prevent coarseness from becoming infinite.

- Contrast

$$contrast = \left(\frac{1}{N_p(1 - N_p)} \sum_{i=1}^{N_g} \sum_{j=1}^{N_g} p(i)p(j)(i-j)^2\right)\left(\frac{1}{N} \sum_{i=1}^{N_g} s(i)\right)$$

- Busyness

$$busyness = \frac{\sum_{i=1}^{N_g} p(i)s(i)}{\sum_{i=1}^{N_g} \sum_{j=1}^{N_g} |ip(i) - jp(j)|}, \qquad p(i) \neq 0, \ p(j) \neq 0$$

- Complexity

$$complexity = \sum_{i=1}^{N_g} \sum_{j=1}^{N_g} |i - j| \frac{p(i)s(i) + p(j)s(j)}{N(p(i) + p(j))}, \qquad p(i) \neq 0, \ p(j) \neq 0$$

- Strength

$$strength = \frac{\sum_{i=1}^{N_g} \sum_{j=1}^{N_g} [p(i) + p(j)](i - j)^2}{\varepsilon + \sum_{n=1}^{N_g} s(i)}, \qquad p(i) \neq 0, \ p(j) \neq 0$$

where ε is a small number to prevent strength from becoming infinite.

References

1. Patel, B.K.; Lobbes, M.; Lewin, J. Contrast Enhanced Spectral Mammography: A Review. *Semin. Ultrasound CT MRI* **2018**, *39*, 70–79. [CrossRef]
2. Heywang-Köbrunner, S.; Viehweg, P.; Heinig, A.; Küchler, C. Contrast-enhanced MRI of the breast: Accuracy, value, controversies, solutions. *Eur. J. Radiol.* **1997**, *24*, 94–108. [CrossRef]
3. Viehweg, P.; Paprosch, I.; Strassinopoulou, M.; Heywang-Köbrunner, S.H. Contrast-enhanced magnetic resonance imaging of the breast: Interpretation guidelines. *Top. Magn. Reson. Imaging* **1998**, *9*, 17–43. [CrossRef] [PubMed]
4. Dromain, C.; Balleyguier, C.; Muller, S.; Mathieu, M.-C.; Rochard, F.; Opolon, P.; Sigal, R. Evaluation of Tumor Angiogenesis of Breast Carcinoma Using Contrast-Enhanced Digital Mammography. *Am. J. Roentgenol.* **2006**, *187*, 528–537. [CrossRef] [PubMed]
5. Baltzer, P.A.; Bickel, H.; Spick, C.; Wengert, G.; Woitek, R.; Kapetas, P.; Clauser, P.; Helbich, T.H.; Pinker, K. Potential of Noncontrast Magnetic Resonance Imaging with Diffusion-Weighted Imaging in Characterization of Breast Lesions. *Investig. Radiol.* **2018**, *53*, 229–235. [CrossRef] [PubMed]
6. Pinker, K.; Moy, L.; Sutton, E.J.; Mann, R.; Weber, M.; Thakur, S.; Jochelson, M.S.; Bago-Horvath, Z.; Morris, E.A.; Baltzer, P.A.; et al. Diffusion-Weighted Imaging with Apparent Diffusion Coefficient Mapping for Breast Cancer Detection as a Stand-Alone Parameter: Comparison with Dynamic Contrast-Enhanced and Multiparametric Magnetic Resonance Imaging. *Investig. Radiol.* **2018**, *53*, 587–595. [CrossRef]
7. Liu, Z.; Feng, B.; Li, C.; Chen, Y.; Chen, Q.; Li, X.; Guan, J.; Chen, X.; Cui, E.; Li, R.; et al. Preoperative prediction of lymphovascular invasion in invasive breast cancer with dynamic contrast-enhanced-MRI-based radiomics. *J. Magn. Reson. Imaging* **2019**, *50*, 847–857. [CrossRef]
8. Li, L.; Roth, R.; Germaine, P.; Ren, S.; Lee, M.; Hunter, K.; Tinney, E.; Liao, L. Contrast-enhanced spectral mammography (CESM) versus breast magnetic resonance imaging (MRI): A retrospective comparison in 66 breast lesions. *Diagn. Interv. Imaging* **2017**, *98*, 113–123. [CrossRef]
9. Fallenberg, E.M.; Dromain, C.; Diekmann, F.; Engelken, F.; Krohn, M.; Singh, J.M.; Ingold-Heppner, B.; Winzer, K.J.; Bick, U.; Renz, D.M. Contrast-enhanced spectral mammography versus MRI: Initial results in the detection of breast cancer and assessment of tumour size. *Eur. Radiol.* **2014**, *24*, 256–264. [CrossRef]
10. Lewin, J.M.; Isaacs, P.K.; Vance, V.; Larke, F.J. Dual-Energy Contrast-enhanced Digital Subtraction Mammography: Feasibility. *Radiology* **2003**, *229*, 261–268. [CrossRef]
11. Jochelson, M.S.; Dershaw, D.D.; Sung, J.; Heerdt, A.; Thornton, C.; Moskowitz, C.S.; Ferrara, J.; Morris, E. Bilateral Contrast-enhanced Dual-Energy Digital Mammography: Feasibility and Comparison with Conventional Digital Mammography and MR Imaging in Women with Known Breast Carcinoma. *Radiology* **2013**, *266*, 743–751. [CrossRef] [PubMed]
12. Tagliafico, A.S.; Bignotti, B.; Rossi, F.; Signori, A.; Sormani, M.P.; Valdora, F.; Calabrese, M.; Houssami, N. Diagnostic performance of contrast-enhanced spectral mammography: Systematic review and meta-analysis. *Breast* **2016**, *28*, 13–19. [CrossRef] [PubMed]
13. Liney, G.P.; Sreenivas, M.; Gibbs, P.; Bsc, R.G.-A.; Turnbull, L.W. Breast lesion analysis of shape technique: Semiautomated vs. manual morphological description. *J. Magn. Reson. Imaging* **2006**, *23*, 493–498. [CrossRef] [PubMed]
14. Fusco, R.; Sansone, M.; Filice, S.; Carone, G.; Amato, D.M.; Sansone, C.; Petrillo, A. Pattern Recognition Approaches for Breast Cancer DCE-MRI Classification: A Systematic Review. *J. Med. Biol. Eng.* **2016**, *36*, 449–459. [CrossRef]
15. Nie, K.; Chen, J.-H.; Yu, H.J.; Chu, Y.; Nalcioglu, O.; Su, M.-Y. Quantitative Analysis of Lesion Morphology and Texture Features for Diagnostic Prediction in Breast MRI. *Acad. Radiol.* **2008**, *15*, 1513–1525. [CrossRef] [PubMed]
16. Hu, H.-T.; Shan, Q.-Y.; Chen, S.-L.; Li, B.; Feng, S.-T.; Xu, E.-J.; Li, X.; Long, J.-Y.; Xie, X.-Y.; Lu, M.-D.; et al. CT-based radiomics for preoperative prediction of early recurrent hepatocellular carcinoma: Technical reproducibility of acquisition and scanners. *Radiol. Med.* **2020**, *125*, 697–705. [CrossRef] [PubMed]
17. Rossi, F.; Bignotti, B.; Bianchi, L.; Picasso, R.; Martinoli, C.; Tagliafico, A.S. Radiomics of peripheral nerves MRI in mild carpal and cubital tunnel syndrome. *Radiol. Med.* **2019**, *125*, 197–203. [CrossRef]
18. Santone, A.; Brunese, M.C.; Donnarumma, F.; Guerriero, P.; Mercaldo, F.; Reginelli, A.; Miele, V.; Giovagnoni, A.; Brunese, L. Radiomic features for prostate cancer grade detection through formal verification. *Radiol. Med.* **2021**, *126*, 688–697. [CrossRef]
19. Fusco, R.; Sansone, M.; Filice, S.; Granata, V.; Catalano, O.; Amato, D.M.; Di Bonito, M.; D'Aiuto, M.; Capasso, I.; Rinaldo, M.; et al. Integration of DCE-MRI and DW-MRI Quantitative Parameters for Breast Lesion Classification. *BioMed Res. Int.* **2015**, *2015*, 237863. [CrossRef]
20. Zhang, Y.; Zhu, Y.; Zhang, K.; Liu, Y.; Cui, J.; Tao, J.; Wang, Y.; Wang, S. Invasive ductal breast cancer: Preoperative predict Ki-67 index based on radiomics of ADC maps. *Radiol. Med.* **2020**, *125*, 109–116. [CrossRef]
21. Chianca, V.; Albano, D.; Messina, C.; Vincenzo, G.; Rizzo, S.; Del Grande, F.; Sconfienza, L.M. An update in musculoskeletal tumors: From quantitative imaging to radiomics. *Radiol. Med.* **2021**, *126*, 1095–1105. [CrossRef] [PubMed]
22. Kirienko, M.; Ninatti, G.; Cozzi, L.; Voulaz, E.; Gennaro, N.; Barajon, I.; Ricci, F.; Carlo-Stella, C.; Zucali, P.; Sollini, M.; et al. Computed tomography (CT)-derived radiomic features differentiate prevascular mediastinum masses as thymic neoplasms versus lymphomas. *Radiol. Med.* **2020**, *125*, 951–960. [CrossRef]
23. Karmazanovsky, G.; Gruzdev, I.; Tikhonova, V.; Kondratyev, E.; Revishvili, A. Computed tomography-based radiomics approach in pancreatic tumors characterization. *Radiol. Med.* **2021**, *126*, 1388–1395. [CrossRef] [PubMed]

24. Cellina, M.; Pirovano, M.; Ciocca, M.; Gibelli, D.; Floridi, C.; Oliva, G. Radiomic analysis of the optic nerve at the first episode of acute optic neuritis: An indicator of optic nerve pathology and a predictor of visual recovery? *Radiol. Med.* **2021**, *126*, 698–706. [CrossRef]

25. Benedetti, G.; Mori, M.; Panzeri, M.M.; Barbera, M.; Palumbo, D.; Sini, C.; Muffatti, F.; Andreasi, V.; Steidler, S.; Doglioni, C.; et al. CT-derived radiomic features to discriminate histologic characteristics of pancreatic neuroendocrine tumors. *Radiol. Med.* **2021**, *126*, 745–760. [CrossRef] [PubMed]

26. Nazari, M.; Shiri, I.; Hajianfar, G.; Oveisi, N.; Abdollahi, H.; Deevband, M.R.; Oveisi, M.; Zaidi, H. Noninvasive Fuhrman grading of clear cell renal cell carcinoma using computed tomography radiomic features and machine learning. *Radiol. Med.* **2020**, *125*, 754–762. [CrossRef] [PubMed]

27. Crivelli, P.; Ledda, R.E.; Parascandolo, N.; Fara, A.; Soro, D.; Conti, M. A New Challenge for Radiologists: Radiomics in Breast Cancer. *BioMed Res. Int.* **2018**, *2018*, 6120703. [CrossRef] [PubMed]

28. Maglogiannis, I.; Zafiropoulos, E.; Anagnostopoulos, I. An intelligent system for automated breast cancer diagnosis and prognosis using SVM based classifiers. *Appl. Intell.* **2007**, *30*, 24–36. [CrossRef]

29. Zheng, Y.; Englander, S.; Baloch, S.; Zacharaki, E.I.; Fan, Y.; Schnall, M.D.; Shen, D. STEP: Spatiotemporal enhancement pattern for MR-based breast tumor diagnosis. *Med. Phys.* **2009**, *36*, 3192–3204. [CrossRef]

30. Lambin, P.; Rios-Velazquez, E.; Leijenaar, R.; Carvalho, S.; van Stiphout, R.G.P.M.; Granton, P.; Zegers, C.M.L.; Gillies, R.; Boellard, R.; Dekker, A.; et al. Radiomics: Extracting more information from medical images using advanced feature analysis. *Eur. J. Cancer* **2012**, *48*, 441–446. [CrossRef]

31. Sinha, S.; Ms, F.A.L.-Q.; Debruhl, N.D.; Sayre, J.; Farria, D.; Gorczyca, D.P.; Bassett, L.W. Multifeature analysis of Gd-enhanced MR images of breast lesions. *J. Magn. Reson. Imaging* **1997**, *7*, 1016–1026. [CrossRef]

32. Vomweg, T.W.; Buscema, P.M.; Kauczor, H.U.; Teifke, A.; Intraligi, M.; Terzi, S.; Heussel, C.P.; Achenbach, T.; Rieker, O.; Mayer, D.; et al. Improved artificial neural networks in prediction of malignancy of lesions in contrast-enhanced MR-mammography. *Med. Phys.* **2003**, *30*, 2350–2359. [CrossRef] [PubMed]

33. Sathya, D.J.; Geetha, K. Mass classification in breast DCE-MR images using an artificial neural network trained via a bee colony optimization algorithm. *ScienceAsia* **2013**, *39*, 294. [CrossRef]

34. Sathya, J.; Geetha, K. Experimental Investigation of Classification Algorithms for Predicting Lesion Type on Breast DCE-MR Images. *Int. J. Comput. Appl.* **2013**, *82*, 1–8. [CrossRef]

35. Fusco, R.; Sansone, M.; Petrillo, A.; Sansone, C. A Multiple Classifier System for Classification of Breast Lesions Using Dynamic and Morphological Features in DCE-MRI. In *Joint IAPR International Workshops on Statistical Techniques in Pattern Recognition (SPR) and Structural and Syntactic Pattern Recognition (SSPR)*; Springer: Berlin/Heidelberg, Germany, 2012; pp. 684–692. [CrossRef]

36. Degenhard, A.; Tanner, C.; Hayes, C.; Hawkes, D.J.; O Leach, M. The UK MRI Breast Screening Study Comparison between radiological and artificial neural network diagnosis in clinical screening. *Physiol. Meas.* **2002**, *23*, 727–739. [CrossRef]

37. Haralick, R.M.; Shanmugam, K.; Dinstein, I.H. Textural Features for Image Classification. *IEEE Trans. Syst. Man Cybern.* **1973**, *SMC-3*, 610–621. [CrossRef]

38. Fusco, R.; Sansone, M.; Sansone, C.; Petrillo, A. Segmentation and classification of breast lesions using dynamic and textural features in Dynamic Contrast Enhanced-Magnetic Resonance Imaging. In Proceedings of the 25th IEEE International Symposium on Computer-Based Medical Systems (CBMS), Rome, Italy, 20–22 June 2012; pp. 1–4.

39. Abdolmaleki, P.; Buadu, L.D.; Naderimansh, H. Feature extraction and classification of breast cancer on dynamic magnetic resonance imaging using artificial neural network. *Cancer Lett.* **2001**, *171*, 183–191. [CrossRef]

40. Agner, S.C.; Soman, S.; Libfeld, E.; McDonald, M.; Thomas, K.; Englander, S.; Rosen, M.A.; Chin, D.; Nosher, J.; Madabhushi, A. Textural Kinetics: A Novel Dynamic Contrast-Enhanced (DCE)-MRI Feature for Breast Lesion Classification. *J. Digit. Imaging* **2010**, *24*, 446–463. [CrossRef]

41. Levman, J.; Leung, T.; Causer, P.; Plewes, D.; Martel, A.L. Classification of dynamic contrast-enhanced magnetic resonance breast lesions by support vector machines. *IEEE Trans. Med. Imaging* **2008**, *27*, 688–696. [CrossRef]

42. Levman, J.; Martel, A.L. Computer-aided diagnosis of breast cancer from magnetic resonance imaging examinations by custom radial basis function vector machine. In Proceedings of the 2010 Annual International Conference of the IEEE Engineering in Medicine and Biology, Buenos Aires, Argentina, 30 August–4 September 2010; Volume 2010, pp. 5577–5580.

43. Fusco, R.; Piccirillo, A.; Sansone, M.; Granata, V.; Rubulotta, M.; Petrosino, T.; Barretta, M.; Vallone, P.; Di Giacomo, R.; Esposito, E.; et al. Radiomics and Artificial Intelligence Analysis with Textural Metrics Extracted by Contrast-Enhanced Mammography in the Breast Lesions Classification. *Diagnostics* **2021**, *11*, 815. [CrossRef]

44. Fusco, R.; Piccirillo, A.; Sansone, M.; Granata, V.; Vallone, P.; Barretta, M.L.; Petrosino, T.; Siani, C.; Di Giacomo, R.; Di Bonito, M.; et al. Radiomic and Artificial Intelligence Analysis with Textural Metrics, Morphological and Dynamic Perfusion Features Extracted by Dynamic Contrast-Enhanced Magnetic Resonance Imaging in the Classification of Breast Lesions. *Appl. Sci.* **2021**, *11*, 1880. [CrossRef]

45. Vallières, M.; Freeman, C.R.; Skamene, S.R.; El Naqa, I. A radiomics model from joint FDG-PET and MRI texture features for the prediction of lung metastases in soft-tissue sarcomas of the extremities. *Phys. Med. Biol.* **2015**, *60*, 5471–5496. [CrossRef]

46. Zwanenburg, A.; Vallières, M.; Abdalah, M.A.; Aerts, H.J.W.L.; Andrearczyk, V.; Apte, A.; Ashrafinia, S.; Bakas, S.; Beukinga, R.J.; Boellaard, R.; et al. The Image Biomarker Standardization Initiative: Standardized Quantitative Radiomics for High-Throughput Image-based Phenotyping. *Radiology* **2020**, *295*, 328–338. [CrossRef]

47. R-Tools Technology Inc. Available online: https://www.r-tt.com/ (accessed on 15 October 2020).

48. Tibshirani, R. The lasso Method for Variable Selection in the Cox Model. *Statist. Med.* **1997**, *16*, 385–395. [CrossRef]

49. Tibshirani, R. Regression Shrinkage and Selection Via the Lasso. *J. R. Stat. Soc. Ser. B Statist. Methodol.* **1996**, *58*, 267–288. [CrossRef]

50. Bruce, P.; Bruce, A. *Practical Statistics for Data Scientists*; O'Reilly Media, Inc.: Newton, MA, USA, 2017.

51. James, G.; Witten, D.; Hastie, T.; Tibshirani, R. *An Introduction to Statistical Learning*; Springer: New York, NY, USA, 2013; Volume 112, p. 18.

52. Wang, Q.; Luo, Z.; Huang, J.; Feng, Y.; Liu, Z. A Novel Ensemble Method for Imbalanced Data Learning: Bagging of Extrapolation-SMOTE SVM. *Comput. Intell. Neurosci.* **2017**, *2017*, 1827016. [CrossRef] [PubMed]

53. Gu, X.; Angelov, P.P.; Soares, E.A. A self-adaptive synthetic over-sampling technique for imbalanced classification. *Int. J. Intell. Syst.* **2020**, *35*, 923–943. [CrossRef]

54. Chen, Z.; Lin, T.; Xia, X.; Xu, H.; Ding, S. A synthetic neighborhood generation-based ensemble learning for the imbalanced data classification. *Appl. Intell.* **2017**, *48*, 2441–2457. [CrossRef]

55. He, H.; Bai, Y.; Garcia, E.A.; Li, S. ADASYN: Adaptive synthetic sampling approach for imbalanced learning. In Proceedings of the 2008 IEEE International Joint Conference on Neural Networks (IEEE World Congress on Computational Intelligence), Hong Kong, China, 1–6 June 2008; pp. 1322–1328.

56. Bernardi, D.; Belli, P.; Benelli, E.; Brancato, B.; Bucchi, L.; Calabrese, M.; Carbonaro, L.A.; Caumo, F.; Cavallo-Marincola, B.; Clauser, P.; et al. Digital breast tomosynthesis (DBT): Recommendations from the Italian College of Breast Radiologists (ICBR) by the Italian Society of Medical Radiology (SIRM) and the Italian Group for Mammography Screening (GISMa). *Radiol. Med.* **2017**, *122*, 723–730. [CrossRef] [PubMed]

57. Bucchi, L.; Belli, P.; Benelli, E.; Bernardi, D.; Brancato, B.; Calabrese, M.; Carbonaro, L.A.; Caumo, F.; Cavallo-Marincola, B.; Clauser, P.; et al. Recommendations for breast imaging follow-up of women with a previous history of breast cancer: Position paper from the Italian Group for Mammography Screening (GISMa) and the Italian College of Breast Radiologists (ICBR) by SIRM. *Radiol. Med.* **2016**, *121*, 891–896. [CrossRef] [PubMed]

58. Losurdo, L.; Fanizzi, A.; Basile, T.M.A.; Bellotti, R.; Bottigli, U.; Dentamaro, R.; Didonna, V.; Lorusso, V.; Massafra, R.; Tamborra, P.; et al. Radiomics Analysis on Contrast-Enhanced Spectral Mammography Images for Breast Cancer Diagnosis: A Pilot Study. *Entropy* **2019**, *21*, 1110. [CrossRef]

59. Fanizzi, A.; Losurdo, L.; Basile, T.M.A.; Bellotti, R.; Bottigli, U.; Delogu, P.; Diacono, D.; Didonna, V.; Fausto, A.; Lombardi, A.; et al. Fully Automated Support System for Diagnosis of Breast Cancer in Contrast-Enhanced Spectral Mammography Images. *J. Clin. Med.* **2019**, *8*, 891. [CrossRef] [PubMed]

60. La Forgia, D.; Fanizzi, A.; Campobasso, F.; Bellotti, R.; Didonna, V.; Lorusso, V.; Moschetta, M.; Massafra, R.; Tamborra, P.; Tangaro, S.; et al. Radiomic Analysis in Contrast-Enhanced Spectral Mammography for Predicting Breast Cancer Histological Outcome. *Diagnostics* **2020**, *10*, 708. [CrossRef] [PubMed]

61. Marino, M.A.; Leithner, D.; Sung, J.; Avendano, D.; Morris, E.A.; Pinker, K.; Jochelson, M.S. Radiomics for Tumor Characterization in Breast Cancer Patients: A Feasibility Study Comparing Contrast-Enhanced Mammography and Magnetic Resonance Imaging. *Diagnostics* **2020**, *10*, 492. [CrossRef]

62. Jiang, T.; Song, J.; Wang, X.; Niu, S.; Zhao, N.; Dong, Y.; Wang, X.; Luo, Y.; Jiang, X. Intratumoral and Peritumoral Analysis of Mammography, Tomosynthesis, and Multiparametric MRI for Predicting Ki-67 Level in Breast Cancer: A Radiomics-Based Study. *Mol. Imaging Biol.* **2021**, 1–10. [CrossRef]

63. Zhao, Y.-F.; Chen, Z.; Zhang, Y.; Zhou, J.; Chen, J.-H.; Lee, K.E.; Combs, F.J.; Parajuli, R.; Mehta, R.S.; Wang, M.; et al. Diagnosis of Breast Cancer Using Radiomics Models Built Based on Dynamic Contrast Enhanced MRI Combined with Mammography. *Front. Oncol.* **2021**, *11*, 774248. [CrossRef]

64. Niu, S.; Wang, X.; Zhao, N.; Liu, G.; Kan, Y.; Dong, Y.; Cui, E.-N.; Luo, Y.; Yu, T.; Jiang, X. Radiomic Evaluations of the Diagnostic Performance of DM, DBT, DCE MRI, DWI, and Their Combination for the Diagnosisof Breast Cancer. *Front. Oncol.* **2021**, *11*, 725922. [CrossRef]